

FERROELECTRICS

Developing fatigue-resistant ferroelectrics using interlayer sliding switching

Renji Bian^{1,2†}, Ri He^{3†}, Er Pan^{1†}, Zefen Li^{1†}, Guiming Cao^{4,5}, Peng Meng¹, Jiangang Chen¹, Qing Liu¹, Zhicheng Zhong^{3,6,7*}, Wenwu Li^{8,9*}, Fucui Liu^{1,2,10*}

Ferroelectric materials have switchable electrical polarization that is appealing for high-density nonvolatile memories. However, inevitable fatigue hinders practical applications of these materials. Fatigue-free ferroelectric switching could dramatically improve the endurance of such devices. We report a fatigue-free ferroelectric system based on the sliding ferroelectricity of bilayer 3R molybdenum disulfide (3R-MoS₂). The memory performance of this ferroelectric device does not show the wake-up effect at low cycles or a substantial fatigue effect after 10⁶ switching cycles under different pulse widths. The total stress time of the device under an electric field is up to 10⁵ s, which is long relative to other devices. Our theoretical calculations reveal that the fatigue-free feature of sliding ferroelectricity is due to the immobile charge defects in sliding ferroelectricity.

Ferroelectric materials have switchable spontaneous polarization that can be flipped by the external electric field and are potentially attractive for nonvolatile memory devices, such as ferroelectric field-effect transistors (FeFETs), ferroelectric tunnel junctions (FTJ), and neuromorphic computers (1–7). The operation of ferroelectric devices is strongly dependent on repeatable bipolar polarization switching. As the number of polarization-reversal cycles increases, the device performance degenerates owing to a reduction of polarization (8–10). This phenomenon is known as ferroelectric fatigue and is widely observed in conventional Pb(Zr,Ti)O₃ (PZT), BiFeO₃ (BFO), BaTiO₃ (BTO), Hf_{0.5}Zr_{0.5}O₂ (HZO), and van der Waals layered CuInP₂S₆ (CIPS) (11–16). This problem seriously hinders these ferroelectric materials from being used in applications. Despite a few decades of research, the origin of this ferroelectric fatigue phenomenon is still not fully understood. Microscopic models suggest that charge defects play a negative role in ferroelectric fatigue (9, 17, 18). Specifically, when a large electric field that is necessary to overcome the potential barrier of different

polarization states is applied to flip the direction of polarization, the charge defects accompany it and then prevent the ferroelectric domain walls from propagating because of the pinning effect (Fig. 1A). So far, several approaches have been proposed to reduce ferroelectric fatigue and rejuvenate fatigue polarization, such as introducing metal oxide as electrodes (19–22), annealing the sample above the Curie temperature, and irradiating with ultraviolet (UV) light (11, 23–25). However, because of the inherited ion-motion nature of ferroelectric switching, the fatigue of ferroelectric polarization inevitably occurs. To address the fatigue issue in conventional ion-type ferroelectric materials, ferroelectric material systems with different switching mechanisms are highly desired.

Sliding ferroelectricity was recently discovered in manually stacked hexagonal boron nitride (h-BN), molybdenum disulfide (MoS₂), molybdenum ditelluride (MoTe₂), and 3R-MoS₂ (26–31). The out-of-plane polarization stems from the interlayer asymmetrically distributed electron charges caused by the special bilayer stacking configurations of two-dimensional

Sliding ferroelectricity was recently discovered in manually stacked hexagonal boron nitride (h-BN), molybdenum disulfide (MoS₂), molybdenum ditelluride (MoTe₂), and 3R-MoS₂ (26–31). The out-of-plane polarization stems from the interlayer asymmetrically distributed electron charges caused by the special bilayer stacking configurations of two-dimensional

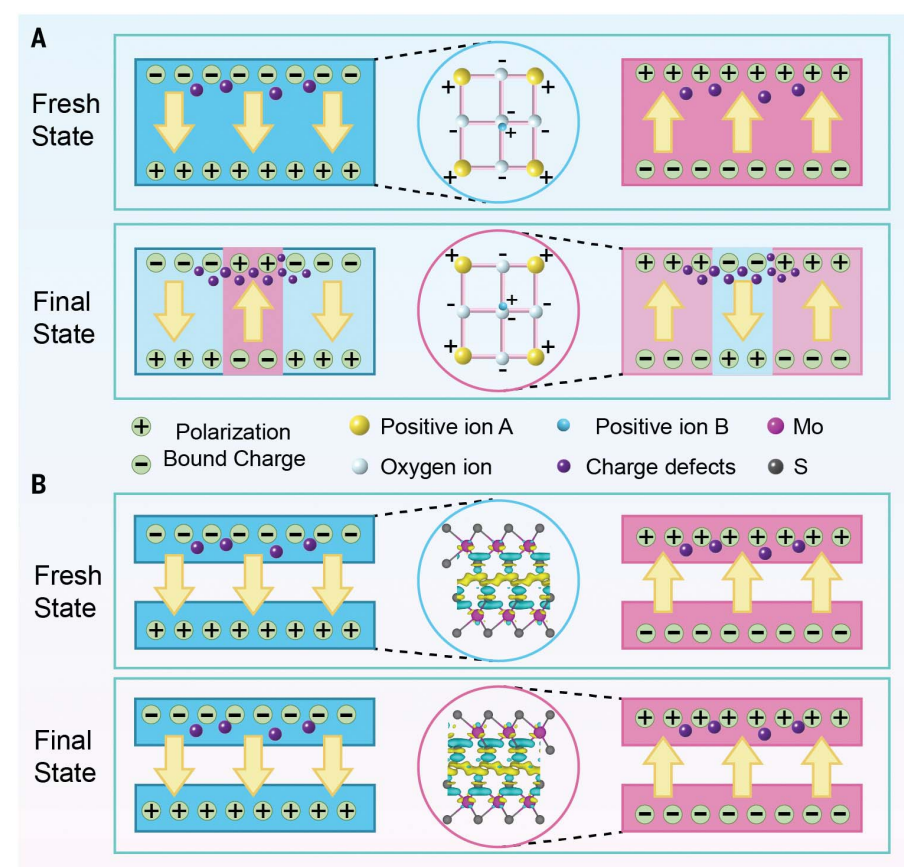


Fig. 1. Difference between conventional ferroelectricity and sliding ferroelectricity after stress.

(A) Schematic of perovskite ferroelectric polarization switching, which is caused by ion displacement and domain-wall pinning by the charge defects, inducing polarization loss. (B) Schematic of sliding ferroelectric polarization-switching mechanism, which is caused by the relative in-plane motion of adjacent layers, thus preventing the charge defects from pinning the polarization at final state. The light-yellow arrows indicate the polarization direction of the domains.

¹School of Optoelectronic Science and Engineering, University of Electronic Science and Technology of China, Chengdu 611731, China. ²Yangtze Delta Region Institute (Huzhou), University of Electronic Science and Technology of China, Huzhou 313001, China. ³Key Laboratory of Magnetic Materials Devices & Zhejiang Province Key Laboratory of Magnetic Materials and Application Technology, Ningbo Institute of Materials Technology and Engineering, Chinese Academy of Sciences, Ningbo 315201, China. ⁴School of Information Science and Technology, Xi Chang University, Xi Chang 615013, China. ⁵Key Laboratory of Liangshan Agriculture Digital Transformation of Sichuan Provincial Education Department, Xi Chang University, Xi Chang 615013, China. ⁶Department of Physics, University of Science and Technology of China, Hefei 230026, China. ⁷Suzhou Institute for Advanced Research, University of Science and Technology of China, Suzhou 215123, China. ⁸Shanghai Frontiers Science Research Base of Intelligent Optoelectronics and Perception, Institute of Optoelectronics, Fudan University, Shanghai 200433, China. ⁹State Key Laboratory of Photovoltaic Science and Technology, Department of Materials Science, Fudan University, Shanghai 200433, China. ¹⁰State Key Laboratory of Electronic Thin Films and Integrated Devices, University of Electronic Science and Technology of China, Chengdu 611731, China.

*Corresponding author. Email: zczhong@ustc.edu.cn (Z.Z.); liwenwu@fudan.edu.cn (W.L.); fucailiu@uestc.edu.cn (F.L.)

†These authors contributed equally to this work.

materials (32, 33). Moreover, the energy barrier for changing stacking configurations is only ~ 8 meV per unit cell (in the case of 3R-MoS₂, fig. S1), which indicates that the electric field can easily drive the relative in-plane motion of adjacent layers to flip the out-of-plane polarization. More importantly, the ferroelectric polarization strength should not be impacted by charge defects because of the migration of charge defects (sulfur vacancies) being strictly in-plane (Fig. 1B). Sliding ferroelectricity may thereby offer an opportunity to overcome the fatigue issue.

We investigated 3R-MoS₂ as an example of a sliding ferroelectric to display its antifatigue properties. We found that whatever pulse widths of the bidirectional sweeping voltage were applied, the polarization switching-associated memory characteristics of 3R-MoS₂ kept almost unchanged, even though stress times were up to 10^5 s. Moreover, we estimated the polarization-switching speed to be about 53 ns. Understanding the static and dynamic properties of the sliding ferroelectric domain wall and the sulfur vacancy defects is critical to unlocking the fatigue-free feature. Considering that such a complex system is beyond the capacity of density functional theory (DFT)

calculation, we constructed a machine learning atomic interaction potential by training a deep neural network on a set of DFT calculations, then carried out the simulation of the domain-wall motion dynamics based on bilayer 3R-MoS₂. Our theoretical calculation suggests that because of the ultralow switching barrier and strong in-plane stiffness of 3R-MoS₂, the charge defects will not aggregate to pin the domain-wall motion when the cyclic electric field repetitively reverses ferroelectric polarization, resulting in the fatigue-free performance of bilayer 3R-MoS₂. Our work demonstrates the potential for sliding ferroelectricity to be a solution to the long-standing fatigue issue in ferroelectric materials.

Van der Waals contact in sliding ferroelectricity

Charge defects in ferroelectric materials are partially attributed to the injection of charge defects from electrodes in ferroelectric devices (9, 18). The creation of a van der Waals contact between the electrode and ferroelectric layer can provide a clean interface to avoid the injection of charge defects into the ferroelectric layer when the cyclic electric field is applied (34). After we confirmed the phase structure

of MoS₂ (fig. S2), a dual-gate device was fabricated, following a schematic of the device structure in which bilayer 3R-MoS₂ is sandwiched between two h-BN molecules and the graphite is used to connect the 3R-MoS₂ channel through a van der Waals contact (Fig. 2A). Figure 2B (inset) shows an optical image of the dual-gate device. We measured the initial electric characteristic of the 3R-MoS₂ device. The output characteristic curve of the device shows a distinct asymmetric feature, in which the drain current quickly gets saturated (20 nA) when the drain voltage increases over 0.1 V, whereas the current increases exponentially as the negative voltage increases, indicating the existence of a back-to-back Schottky barrier (35, 36). In addition, similarly to the 2H-stacked MoS₂, the bilayer 3R-MoS₂ exhibits the semiconducting feature with a bandgap of 1.26 eV, suggesting that its conductivity can be modulated by the electrostatic gate (37). We observed the n-type nature of the 3R-MoS₂ from the transfer characteristic curve (Fig. 2C and fig. S3); the current on/off ratio of the device is 10^6 .

To confirm the ferroelectricity of 3R-MoS₂, we conducted both dynamic and static electrical

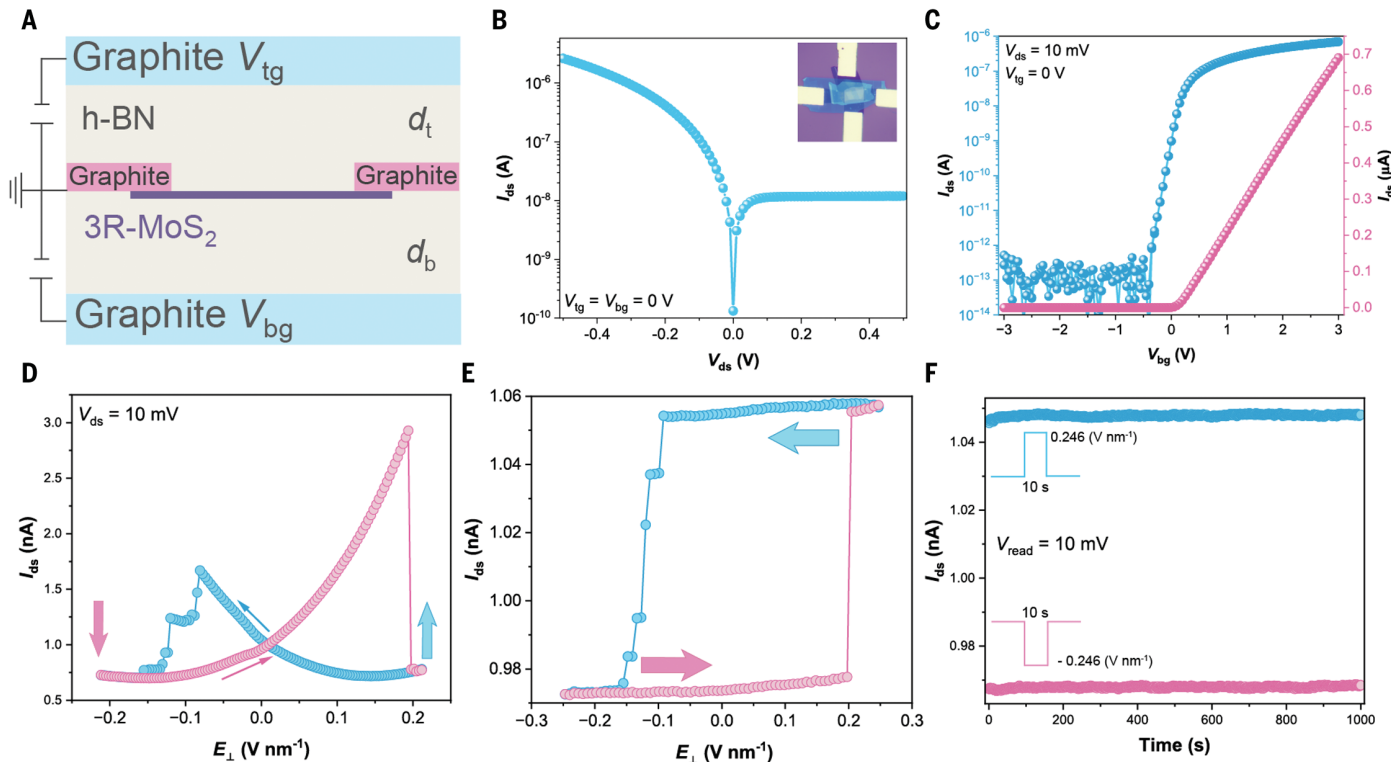


Fig. 2. Electric characteristic of the 3R-MoS₂ device. (A) Schematic cross-section of bilayer 3R-MoS₂ dual-gate device. (B) Output curve of the device under top gate with back gate grounded, where the asymmetric electric curve shows the distinct Schottky barrier. (Inset) Optical image of a dual-gate device. (C) Back-gate transfer curve of the device, in which the drain voltage is fixed at 10 mV and the top gate is grounded to avoid capacitance coupling. (D) Dynamic ferroelectric electric transport, where the drain current is a function of E_{\perp} , the

top-gate and back-gate voltage is set to $V_{tg}/d_t = -V_{bg}/d_b$, and the upward electric field direction is from back gate to top gate. The small blue arrow and pink arrow show the hysteresis direction as the electric field sweeps. (E) Static ferroelectric electric transport, where the drain current is a function of the electric field pulse train (as shown in fig. S4). (F) Retention properties of the bistate after setting by applying an electric field of 0.246 V nm^{-1} and -0.246 V nm^{-1} with a pulse width of 10 s.

measurements. For the dynamic electrical measurement, we applied a continuous vertical electric field of $E_{\perp} = (-V_{\text{tg}}/d_t + V_{\text{bg}}/d_b)/2$, where the back-gate voltage, V_{bg} , is linearly proportional to the top-gate voltage, $V_{\text{tg}}[V_{\text{bg}} = -\alpha V_{\text{tg}} (\alpha = d_b/d_t)]$, to avoid the net carrier doping in the channel (the drain current of the device as a function of the sweeping electric field is shown in Fig. 2D). We observed a typical butterfly curve while the electric field scanned from downward to upward and back to downward, which is consistent with previous works (27, 38). We attribute the sudden drop of the drain current to the electron flowing along the channel perturbed by the switching of the internal electric field induced by

the external electric field (38). To preclude other mechanisms for the drain-current change, we conducted the gate-scanning rate-dependent measurement (fig. S4). For the static electrical measurement, we applied a vertical scanning pulsed electric field with a period of 5 s (fig. S5), and we recorded the drain current after each pulsed electric field stimulus. The electrical curve we obtained displays a typical rectangular hysteresis loop (Fig. 2E). During the pulsed electric field forward scanning, we set the device to the low-resistance state (LRS), about 1.05 nA once the electric field increased to 0.246 V nm^{-1} . The drain current kept stable until the electric field was backward scanned to -0.08 V nm^{-1} , then it suddenly dropped to a high-resistance

state (HRS) with the electric field decreasing to -0.18 V nm^{-1} . The retention property of LRS and HRS was tested by applying an electric field of 0.246 V nm^{-1} and -0.246 V nm^{-1} to set and reset the device, respectively. The LRS and HRS were obviously distinguished after 1000 s (Fig. 2F), indicating that the polarization has a stable nonvolatility. In addition, we also confirmed the ferroelectricity of bilayer 3R-MoS₂ with the hysteresis loop measurement using switching spectroscopy piezoresponse force microscopy (SS-PFM) (fig. S6).

Fatigue performance of the 3R-MoS₂ device

To provide insight into the endurance of the polarization switching of sliding ferroelectricity,

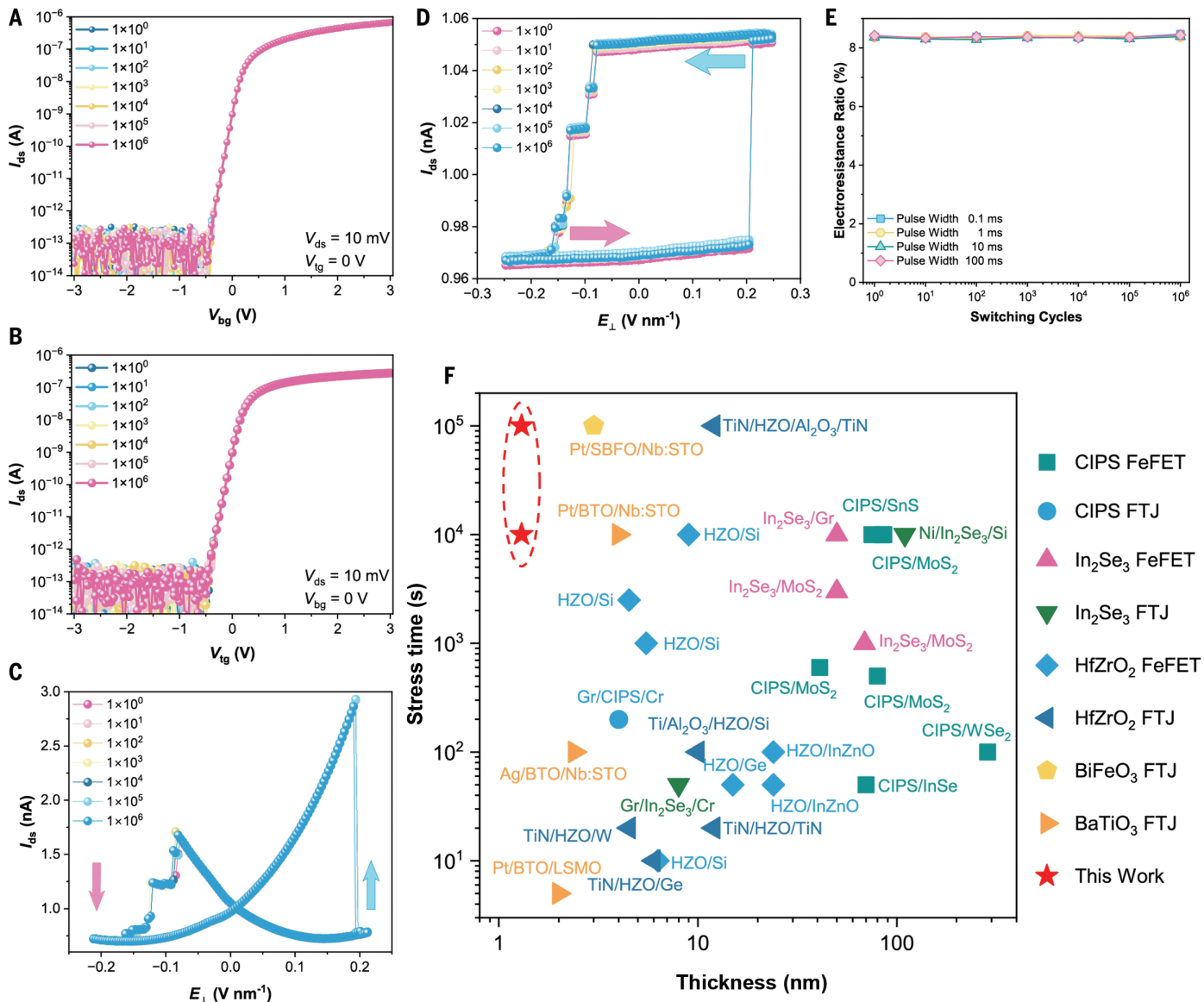


Fig. 3. Fatigue characteristics of the 3R-MoS₂ device. (A) Coincident back-gate and (B) top-gate transfer curves, which represent the high reliability of transistor performance. (C) Dynamic and (D) static ferroelectric electric transport curves, indicating the device's superior antifatigue feature.

(E) Electroresistance ratio cycle at various pulse widths and cycle numbers. (F) Comparison of typical ferroelectric devices as a function of thickness and total stress time. Details of the device information and related references are listed in table S1.

we designed periodic bipolar pulses with different widths to flip the polarization direction of 3R-MoS₂ repeatedly (fig. S7). After each order of magnitude of cycle testing, we recorded the transfer characteristic and ferroelectric hysteresis curves by performing the back- and top-gate sweeping voltage. We found that the back- and top-gate tuned transfer characteristics of the device (Fig. 3, A and B) are almost coincident even when polarization has been switched for 10⁶ cycles. This indicates that the electrical characteristics of our 3R-MoS₂ device are highly reliable for performing fatigue tests. During the 10⁶-cycle measurement, the dynamic and static electrical curves of the 3R-MoS₂ device were nearly overlapped (Fig. 3, C and D), indicating that the switchable polarization dipoles do not display an identifiable loss. We obtained a value of 8% electroresistance ratio (Fig. 3E), $\{ER = [I_{(on)} - I_{(off)}]/I_{(off)}\}$, that we extracted from static transport, which was almost unchanged while the cyclic number increased to 10⁶. This indicates that the sliding ferroelectric device does not show a wake-up effect or fatigue. Similar results were observed in one additional device (fig. S8).

In conventional ferroelectricity, the fatigue strongly depends on the duration of applied pulses because the charge defects can migrate along the electric field, particularly when the duration of the write operation is long (39). This results in a more obvious screening or pinning effect on ferroelectric polarization. Thus, the pulse width should also be considered to evaluate the endurance performance of sliding ferroelectricity. As the pulse width ranged from 1 to 100 ms, the transfer characteristics and ferroelectric hysteresis curves did not display any changes when the testing cycles were increased to 10⁶ (figs. S9 to S11). To evaluate the performance of ferroelectricity, the total stress time (pulse number multiplied by pulse width) should be used to estimate the endurance performance of ferroelectricity. We summarize the total stress time-dependent fatigue performance of sliding ferroelectricity and conventional ferroelectricity in Fig. 3F and table S1. Our 1.3-nm-thick 3R-MoS₂ displayed a stress time of up to 10⁵ s, which is superior to that of most traditional ferroelectric materials. In addition, we used Kelvin probe force microscopy (KPFM) to characterize the fatigue performance of the local polarization in 3R-MoS₂. A large-scale 3R-MoS₂ flake showed domains with potential difference (fig. S12, A and B). To measure the fatigue, we selected the area marked as a red box in fig. S12C. After we stressed our sample to 10⁴ cycles, we did not observe degeneration or damage (see topography and surface potential images in fig. S12, D and F; details of the measurement procedure and analysis are described in the caption of fig. S12).

Theoretical analysis of the antifatigue performance of 3R-MoS₂

Microscopic fatigue models have highlighted that the accumulation of charge defects of oxygen vacancy in perovskite ferroelectricity under a cyclic electric field will induce domain-nucleation inhibition and domain-wall pinning (9, 17). In the case of ferroelectric MoS₂, we identified the dominant charge defects as the sulfur vacancies with one (Vs₁) or two (Vs₂) sulfur atoms absent (40) (fig. S13). Hence, to reveal the antifatigue performance of sliding ferroelectricity on the basis of 3R-MoS₂, we analyzed the effect of sulfur vacancies. We set the bilayer 3R-MoS₂ containing Vs₁ to the initial state (Fig. 4A), in which the migration of sulfur vacancy along the vertical electric field has two opposite pathways. Path 1 shows that the sulfur vacancy moves from bottom to top in an individual layer of MoS₂, in which the energy barrier is about 2.6 eV from DFT calculations. Path 2 indicates that the sulfur vacancy diffuses across the van der Waals gap, where the energy barrier is up to 4.6 eV. Com-

pared with the 136-meV switching barrier (fig. S14), the high-energy barriers of Path 1 and Path 2 suggest that the redistribution of sulfur vacancy would not inhibit the domain nucleation or pin the domain-wall motion when the cyclic electric field is applied to the sliding ferroelectricity to switch its polarization direction. To gain further insight into the fatigue-free features of sliding ferroelectricity, we verified whether the immobile sulfur vacancies could be attributed to the domain-nucleation inhibition or to domain-wall pinning. First, domain-nucleation inhibition by the charge defects can be ignored because the switchable polarization is mainly triggered through the motion of the domain wall instead of the formation of the domain nucleus, which we confirmed with our experiments and simulations (figs. S15 and S16). Having established the switching mechanism, we constructed a large supercell containing sulfur vacancies (Vs₁) to investigate its pinning effect on domain-wall motion. The machine learning-assisted molecular dynamic simulation showed that the domain wall could smoothly

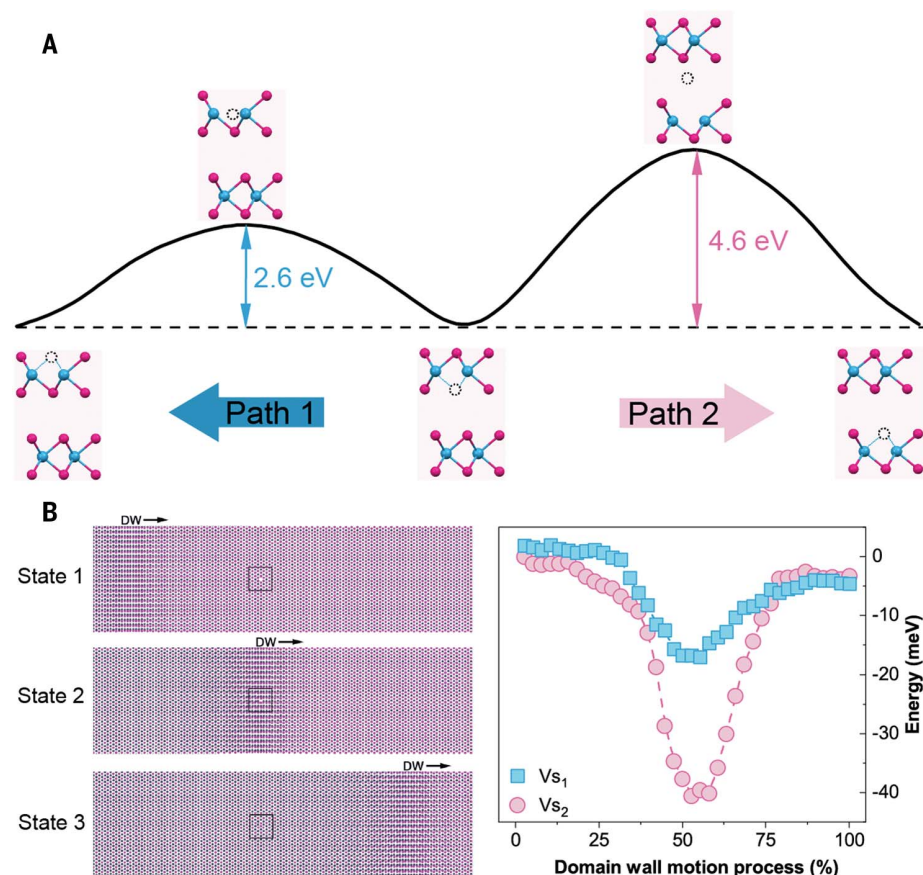
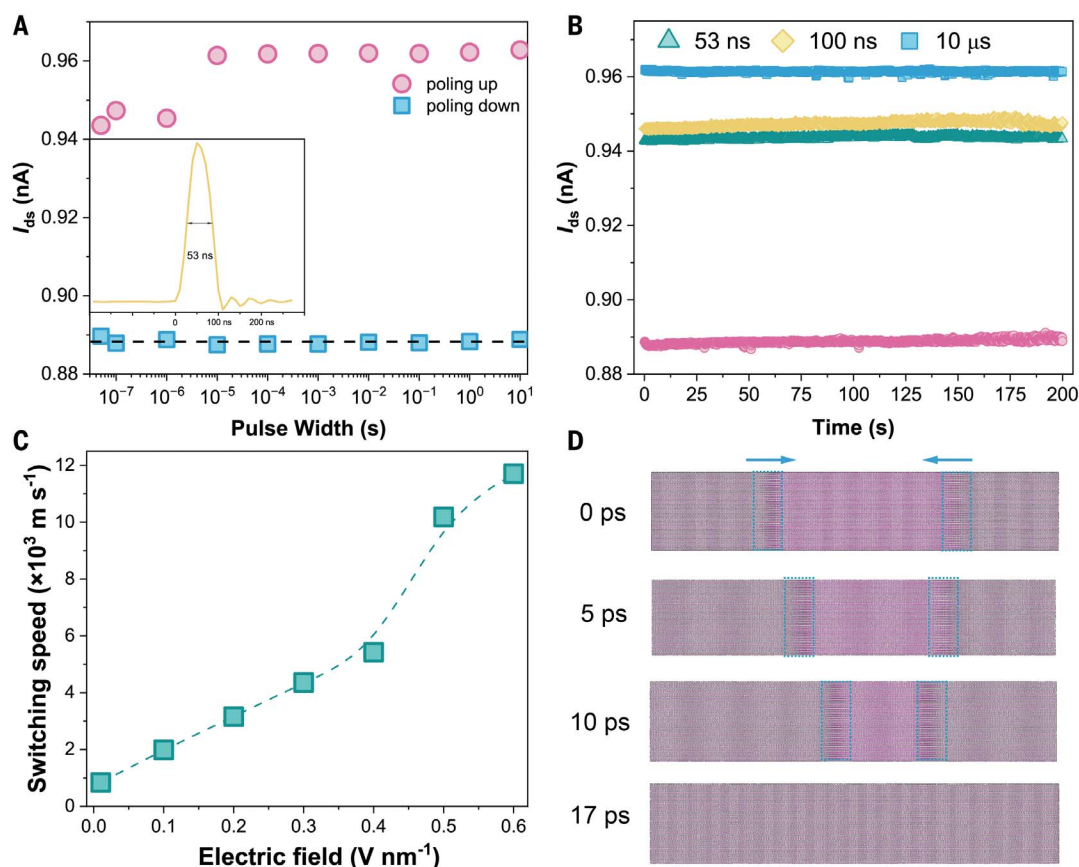


Fig. 4. Theoretical analysis of antifatigue performance of 3R-MoS₂. (A) Illustrations of the sulfur-vacancy diffusion paths and corresponding energy barriers. Path 1 indicates that the sulfur vacancy migrates in the individual layer, whereas Path 2 indicates that the sulfur vacancy migrates across the van der Waals gap. The blue spheres are molybdenum atoms, and the red spheres are sulfur atoms. The dashed black circle represents the sulfur vacancy. (B) Atomic structure of supercell containing a sulfur vacancy at different positions of the domain wall. The energy profile of the domain wall approaches and moves away from the sulfur vacancy calculated by machine learning potential containing one or two sulfur vacancies. The black square represents the sulfur vacancy.

Fig. 5. Ultrafast switching of the 3R-MoS₂ device. (A) Device programming speed with fixed HRS; a pulse width as low as 53 ns can implement effective writing, which is attributed to the device's ultrafast ferroelectric switching (inset shows a waveform of a 53-ns ultrafast write pulse). (B) Under the action of pulse widths of 53 ns, 100 ns and 10 μ s (0.246 V nm⁻¹) write pulse, the drain current changes and shows nonvolatile data retention, confirming the ultrafast programmability of the sliding ferroelectric transistor. (C) Average domain-switching speed at various electric field values. (D) Time-dependent simulations of domain-wall motion of bilayer 3R-MoS₂ at 0, 5, 10, and 17 ps, where the cyan rectangle represents the domain wall and the cyan arrow indicates the direction of motion of the domain wall.



move across the sulfur vacancy under an electric field of 0.2 V nm⁻¹ (Fig. 4B, left panel). We adopted the machine learning potential to quantitatively describe the system energy of the supercell containing sulfur vacancies at different positions of the domain wall. When the domain wall was close to the sulfur vacancy, the energy decreased to -15 meV (Fig. 4B). This means that the domain wall drops into a potential well. However, the energy was too weak to trap the domain-wall motion, which we confirmed by the critical electric fields of domain-wall motion with and without sulfur vacancy, at 0.11 and 0.13 V nm⁻¹. The potential well energy increased to 40 meV while the supercell contained Vs₂, suggesting that more sulfur vacancies tend to trap the domain wall. Then we further performed molecular dynamics simulations of bilayer 3R-MoS₂ with more sulfur vacancies. We found that more sulfur vacancies do not migrate or aggregate under the cyclic electric field or pin the domain-wall motion at temperatures up to 500 K (figs. S17 and S18), indicating the anti-fatigue property of 3R-MoS₂ ferroelectricity.

Ultrafast switching of sliding ferroelectricity based on 3R-MoS₂

To characterize the switching speed of the 3R-MoS₂ ferroelectric device, we implemented the voltage pulse with various widths as a poling electric field. During the measurement, we first

set the device to the HRS by applying an electric field pulse of -0.246 V nm⁻¹ with a duration of 10 s. Then we separately applied an electric field of 0.246 V nm⁻¹ with a duration ranging from 53 ns to 10 s. Subsequently, we recorded the drain current at a bias of 0.01 V. We obtained an obvious LRS even when the pulse width was as low as 53 ns (Fig. 5A), which was further confirmed by the retention characteristics of the LRS (Fig. 5B). We further investigated the limiting speed of sliding ferroelectric polarization switching with molecular dynamic simulations (Fig. 5C). While applying an electric field at 300 K, we observed a soliton-like motion of domain walls. After 17 ps, the domain wall annihilated into a single domain (Fig. 5D, bottom panel). When the electric field was 0.2 V nm⁻¹, the BA domain grew linearly with time. The constant domain-wall velocity of 3000 m s⁻¹ indicates that the switching time is about 0.3 ns for a 1000-nm-diameter domain. This feature of ultrafast domain-wall motion is promising for applications in ultrafast nonvolatile memory devices.

Discussion

The ferroelectric memory device transistor based on sliding ferroelectricity shows an outstanding antifatigue performance of up to 10⁵ s stress time. Furthermore, the fatigue is almost independent of the pulse width and totally different from that of traditional ferroelectric

oxide. Our calculations show that the fatigue-free feature can be attributed to the comprehensive influence of three aspects: the immobility of charge defects during polarization switching, the negligible pinning effect of charge defects on domain-wall motions, and the ultra-low polarization-switching barrier. Therefore, it is reasonable to presume that the fatigue-free feature is an intrinsic property of sliding ferroelectricity. This feature can help to overcome the key obstacle to the practical use of ferroelectric devices. Moreover, the switchable dipole combined with the semiconducting and valleytronic features of 3R-MoS₂ will pave the way for many new applications for these devices.

REFERENCES AND NOTES

1. M. Si et al., *Nat. Electron.* **2**, 580–586 (2019).
2. A. I. Khan, A. Keshavarzi, S. Datta, *Nat. Electron.* **3**, 588–597 (2020).
3. J. Wu et al., *Nat. Electron.* **3**, 466–472 (2020).
4. T. Mikolajick et al., *J. Appl. Phys.* **129**, 100901 (2021).
5. L. W. Martin, A. M. Rappe, *Nat. Rev. Mater.* **2**, 16087 (2017).
6. S. Kamaei et al., *Nat. Electron.* **6**, 658–668 (2023).
7. S. Wang et al., *Nat. Commun.* **12**, 53 (2021).
8. P. J. Schorn et al., *J. Appl. Phys.* **99**, 114104 (2006).
9. A. K. Tagantsev, I. Stolichev, E. Colla, N. Setter, *J. Appl. Phys.* **90**, 1387–1402 (2001).
10. W. L. Warren et al., *J. Appl. Phys.* **77**, 6695–6702 (1995).
11. W. L. Warren, D. Dimos, B. A. Tuttle, R. D. Nasby, G. E. Pike, *Appl. Phys. Lett.* **65**, 1018–1020 (1994).
12. Y. Yang et al., *Sci. Adv.* **7**, eabh2716 (2021).
13. Y. Wei et al., *Nat. Mater.* **17**, 1095–1100 (2018).
14. F. Liu et al., *Nat. Commun.* **7**, 12357 (2016).

15. T. Choi, S. Lee, Y. J. Choi, V. Kiryukhin, S.-W. Cheong, *Science* **324**, 63–66 (2009).
16. Z. Zhou et al., *Nat. Commun.* **14**, 8254 (2023).
17. Q. Huang et al., *Nat. Commun.* **12**, 2095 (2021).
18. A. V. Ilev et al., *Nat. Commun.* **10**, 3064 (2019).
19. M. S. Chen, T. B. Wu, J. M. Wu, *Appl. Phys. Lett.* **68**, 1430–1432 (1996).
20. C. B. Eom et al., *Appl. Phys. Lett.* **63**, 2570–2572 (1993).
21. R. Ramesh et al., *Appl. Phys. Lett.* **63**, 3592–3594 (1993).
22. W. Wu, K. H. Wong, C. L. Choy, Y. H. Zhang, *Appl. Phys. Lett.* **77**, 3441–3443 (2000).
23. S. S. Fu, H. Yu, X. Y. Luo, Y. L. Jiang, G. D. Zhu, *IEEE Electron Device Lett.* **33**, 95–97 (2012).
24. F. Huang et al., *Phys. Chem. Chem. Phys.* **19**, 3486–3497 (2017).
25. C. Verdier, D. C. Lupascu, H. von Seggern, J. Rödel, *Appl. Phys. Lett.* **85**, 3211–3213 (2004).
26. K. Yasuda, X. Wang, K. Watanabe, T. Taniguchi, P. Jarillo-Herrero, *Science* **372**, 1458–1462 (2021).
27. M. Vizner Stern et al., *Science* **372**, 1462–1466 (2021).
28. P. Meng et al., *Nat. Commun.* **13**, 7696 (2022).
29. X. Wang et al., *Nat. Nanotechnol.* **17**, 367–371 (2022).
30. A. Weston et al., *Nat. Nanotechnol.* **17**, 390–395 (2022).
31. A. Jindal et al., *Nature* **613**, 48–52 (2023).
32. L. Li, M. Wu, *ACS Nano* **11**, 6382–6388 (2017).
33. M. Wu, J. Li, *Proc. Natl. Acad. Sci. U.S.A.* **118**, e2115703118 (2021).
34. Y. Liu et al., *Nature* **557**, 696–700 (2018).
35. C. Marquez et al., *2D Mater.* **7**, 025040 (2020).
36. A. Di Bartolomeo et al., *Adv. Funct. Mater.* **28**, 1800657 (2018).
37. I. A. Rahman, A. Purqon, *J. Phys. Conf. Ser.* **877**, 012026 (2017).
38. Y. A. Eshete et al., *Adv. Mater.* **34**, e2202633 (2022).
39. L. Pintilie, I. Vrejoiu, D. Hesse, M. Alexe, *Appl. Phys. Lett.* **88**, 102908 (2006).
40. J. Hong et al., *Nat. Commun.* **6**, 6293 (2015).

ACKNOWLEDGMENTS

We thank T. Zhou and A. Zhou from the Analysis and Testing Center at the University of Electronic Science and Technology of China for technical support. **Funding:** This work was supported by the National Natural Science Foundation of China (12161141015, 62074025, 62304183, 62374043, 12204496, and 51931011), the National Key Research and Development Program (2021YFE0194200 and 2020YFA0309200), the Sichuan Science and Technology Program (2024YFHZ0264), the Sichuan Province Key Laboratory of Display Science and Technology, Shanghai Oriental Talent Program-Youth Project (2022), and the Zhejiang Provincial Natural Science Foundation (Q23A040003). **Author contributions:** F.L., Z.Z., and W.L. supervised the project. F.L., R.B., and R.H. conceived the idea and designed the experiments. R.B. fabricated the dual-gate field-effect transistor, performed the electronic transport measurements, and analyzed the data, with the assistance of E.P.

and Z.L. R.H. and Z.Z. performed the DFT calculations, molecular dynamic simulations, and theoretical analysis. Z.L. and Q.L. synthesized the 3R-MoS₂ crystal and conducted the material characterization. E.P. and Z.L. performed the KPFM and SS-PFM measurements. P.M., G.C., J.C., and W.L. analyzed the data. R.B., R.H., F.L., W.L., and Z.Z. wrote the manuscript with input from all authors. All authors discussed the results. **Competing interests:** The authors declare that they have no competing interests. **Data and materials availability:** All data are available in the main text or the supplementary material. **License information:** Copyright © 2024 the authors, some rights reserved; exclusive licensee American Association for the Advancement of Science. No claim to original US government works. <https://www.science.org/about/science-licenses-journal-article-reuse>

SUPPLEMENTARY MATERIALS

science.org/doi/10.1126/science.ado1744
 Materials and Methods
 Supplementary Text
 Figs. S1 to S21
 Table S1
 References (41–71)
 Movie S1
 Data S1 and S2
 Submitted 19 January 2024; accepted 24 May 2024
 Published online 6 June 2024
[10.1126/science.ado1744](https://doi.org/10.1126/science.ado1744)